

Combined LOFAR-uGMRT analysis of the diffuse radio emission in the massive clusters Abell 773 and Abell 1351

K. S. L. Srikanth^{1,2}, A. Botteon¹, R. Cassano¹, G. Brunetti¹, A. Bonafede^{1,2}, L. Bruno¹, M. Balboni^{2,3}, H. Bashir⁹, M. Brüggen⁴, S. Chatterjee⁵, V. Cuciti^{1,2}, D. Dallacasa^{1,2}, A. Datta¹¹, F. de Gasperin¹, G. Di Gennaro¹, C. Groeneveld^{1,6}, R. Kale⁸, M. A. Malik⁹, S. Paul¹⁰, S. Salunkhe⁸, R. J. van Weeren⁶, T. Venturi^{1,5}, and X. Zhang⁷

¹ Istituto Nazionale di Astrofisica (INAF) - Istituto di Radioastronomia (IRA), via Gobetti 101, 40129 Bologna, Italy

² Dipartimento di Fisica e Astronomia (DIFA), Università di Bologna, via Gobetti 93/2, 40129 Bologna, Italy

³ Istituto Nazionale di Astrofisica – Istituto di Astrofisica Spaziale e Fisica Cosmica (IASF), Via A. Corti 12, 20133 Milano, Italy

⁴ Hamburger Sternwarte, Universität Hamburg, Gojenbergsweg 112, 21029 Hamburg, Germany

⁵ Center for Radio Astronomy Techniques and Technologies, Rhodes University, Grahamstown 6140, South Africa

⁶ Leiden Observatory, Leiden University, PO Box 9513, 2300 RA Leiden, The Netherlands

⁷ Max-Planck-Institut für Extraterrestrische Physik (MPE), Gießenbachstraße 1, D-85748 Garching bei München, Germany

⁸ National Centre for Radio Astrophysics, Tata Institute of Fundamental Research, S. P. Pune University Campus, Ganeshkhind, Pune 411007, India

⁹ University of Kashmir, Hazratbal, Srinagar, J&K, India – 190006

¹⁰ Manipal Centre for Natural Sciences, Manipal Academy of Higher Education, Karnataka, Manipal - 576104, India

¹¹ Indian Institute of Technology Indore, Indore-453552, M.P., India.

e-mail: koushikasri.srikanth2@unibo.it

January 15, 2026

ABSTRACT

Context. Radio halos are megaparsec-scale diffuse, non-thermal radio sources located at the center of galaxy clusters. They trace relativistic particles and magnetic fields in the intra-cluster medium. The source of energy for their formation is believed to be the merging of galaxy clusters, which generates turbulence and re-accelerates aged electrons.

Aims. We aim to study the diffuse radio emission, spectral properties and connection between thermal and non- thermal emission in the massive ($M_{500} \sim 7 \times 10^{14} M_{\odot}$), dynamically disturbed galaxy clusters Abell 773 and Abell 1351.

Methods. We combine observations from the LOFAR Two-meter Sky Survey - Data Release 2 (LoTSS-DR2) at 144 MHz and the new upgraded Giant Meterwave Radio Telescope (uGMRT) at 650 MHz for both clusters. Additionally, archival *XMM-Newton* X-ray images are utilized to supplement our analysis.

Results. We confirm that both clusters host a radio halo, extending up to a largest linear size (LLS) of ~ 2 Mpc. We measure an integrated spectral index α_{144}^{650} of ~ -1.0 for both the clusters. We show that radio halo in A773 resembles a classical radio halo that follows a sublinear relation in point-to-point analysis between radio and X-ray surface brightness. Conversely, A1351 exhibits a more complex and asymmetric radio halo, embedded by several radio sources, including the bright cluster galaxy (BCG), a tail galaxy (TG), and the ridge. We found a deviation from the sublinear relation in the point-to-point analysis of A1351 due to the presence of these contaminating radio sources.

Key words. galaxies: clusters: individual: A773, A1351 - galaxies: clusters: intracluster medium - radiation mechanisms: non-thermal

1. Introduction

Galaxy clusters are gravitationally bound structures with a mass $\sim 10^{14} - 10^{15} M_{\odot}$. According to the Lambda Cold Dark Matter (Λ CDM) model, clusters form hierarchically through sequence of mergers and accretion of smaller systems over a timescale of about $10^9 \sim 10^{10}$ years (Press & Schechter 1974; Springel et al. 2006). The space between the galaxies is filled by the hot intra-cluster medium (ICM), a plasma with a temperature of $\sim 10^7 - 10^8$ K. Mergers between galaxy clusters are the most energetic events in the Universe. While most of this energy contributes to the heating of the ICM, part of it is also channelled into the acceleration of relativistic particles via shocks and turbulence and amplification of magnetic fields (Markevitch & Vikhlinin 2007).

Radio observations of galaxy clusters have uncovered large-scale, diffuse synchrotron sources that trace the presence of relativistic particles and magnetic fields in the ICM. These sources are classified as radio relics and radio halos, respectively located at the peripheries and centers of merging clusters, and mini-halos surrounding the cool core region of the relaxed clusters (van Weeren et al. 2019). Among these, radio haloes (RHs) often extend up to \sim Mpc scales and are likely powered by turbulent re-acceleration process within the ICM (Brunetti & Jones 2014). An alternative explanation is that radio halos form as synchrotron emission by secondary electrons generated by proton-proton collisions in the ICM (Dennison 1980; Blasi & Colafrancesco 1999; Dolag & Enßlin 2000). However, the lack of γ -ray detections from galaxy cluster observations expected as by-product of the proton-proton collisions (Brunetti et al. 2017; Adam et al. 2021) and the existence of radio halos with

very steep radio spectra ($\alpha < 1$, where $f(\nu) \propto \nu^\alpha$) (Brunetti et al. 2008; Wilber et al. 2018; Di Gennaro et al. 2021; Bruno et al. 2021; Pasini et al. 2024; Osinga et al. 2024; Santra et al. 2024) disfavor hadronic models as the primary mechanism for their origin. This is further supported by the sublinear point-to-point correlations observed between the radio and X-ray surface brightness in clusters hosting radio halos (Govoni et al. 2001a; Brunetti & Jones 2014). Such correlations suggest that the non-thermal components exhibit a weak radial decline with respect to the thermal gas (Balboni et al. 2024). In re-acceleration models, the energy available for turbulent re-acceleration comes from the dissipation of gravitational energy of mergers, and hence a correlation between the occurrence of radio halos and the cluster mass and dynamics is expected (Cassano & Brunetti 2005; Cassano 2010; Wen & Han 2013; Giacintucci et al. 2017). Furthermore, several studies have revealed that the majority of RHs are found in merging clusters, whereas clusters without diffuse emission are typically in a relaxed state (Cassano et al. 2010; Kale et al. 2015; Venturi et al. 2007, 2008; Cassano et al. 2013, 2023).

A key prediction of turbulent re-acceleration models is that a large fraction of halos should have very steep spectra, being generated during less energetic merger events (i.e.; minor mergers or major mergers between less massive clusters) where the turbulent energy may not be enough to accelerate electrons up to the energy required to generate synchrotron radiation at GHz frequencies (Cassano et al. 2006; Brunetti et al. 2008). Recent statistical studies at low frequency with LOFAR have indeed identified RHs also in less disturbed clusters (Cassano et al. 2023). Additionally, there is evidence of cluster-scale diffuse emission in cool-core clusters (Bonafede et al. 2014; Savini et al. 2018; Biava et al. 2024; van Weeren et al. 2024). In this paper, we focus on the study of two massive and optically rich galaxy clusters, PSZ2 G166.09+43.38 (also known as A773) and PSZ2 G139.18+56.37 (also known as A1351), both hosting giant RH. The clusters were observed using the LOw Frequency AR-ray High Band Antenna (LOFAR-HBA; 120–168 MHz) and the upgraded Giant Metrewave Radio Telescope Band 4 (uGMRT Band 4; 550–750 MHz). The physical properties of the clusters are listed in Table 1. From X-ray analysis both A773 and A1351 are identified as merging clusters but in different merger states. Chandra X-ray observations reveal that A773 is an advanced merger (Barrena et al. 2007). A1351, on the other hand, is an ongoing merger (Allen et al. 2003; Giovannini et al. 2009; Giacintucci et al. 2009; Barrena et al. 2014), a scenario further supported by weak-lensing analyses from Holjhjem et al. (2009). The presence of a giant RH in A773 (~ 1.6 Mpc) was first reported by Govoni et al. (2001b) using Very Large Array (VLA) observations at 1.4 GHz in C and D configurations. The diffuse radio emission in A1351 was initially detected by Owen et al. (1999), and later VLA observations at 1.4 GHz by Giacintucci et al. (2009) confirmed a giant RH with an extent of ~ 1.1 Mpc. More recently, Chatterjee et al. (2022) used GMRT (610 MHz) and VLA (1.4 GHz) observations to provide additional insights into the RH structure and the radio ridge in A1351.

This paper is structured as follows: In Section 2, we describe the radio observations, data reduction, and analysis. Section 3 presents the results obtained from the radio observations. A discussion of these results is provided in Section 4, followed by a summary and conclusions in Section 5.

Throughout this work, we adopt a standard Λ CDM cosmology with $H_0 = 70 \text{ km s}^{-1} \text{ Mpc}^{-1}$, $\Omega_M = 0.3$, and $\Omega_\Lambda = 0.70$.

2. Radio observation and data analysis

2.1. LOFAR observations

The clusters A773 & A1351 were observed as part of the LoTSS-DR2 survey (Shimwell et al. 2022)¹ which covers 27% of the northern sky in the frequency range of 120–168 MHz (central frequency 144 MHz). Each LoTSS pointing lasts 8 hours, achieving a median root-mean-square (σ_{rms}) sensitivity of $\sim 0.1 \text{ mJy beam}^{-1}$ at a resolution of $6''$ (Shimwell et al. 2019). We utilized the data processed by Botteon et al. (2022) in their study to search for radio halos in the Planck clusters within the LoTSS-DR2 survey. For detailed information on the data processing of the clusters in LoTSS-DR2, we refer the reader to Shimwell et al. (2019); Shimwell et al. (2022) and Tasse et al. (2021), which describe the Survey Key Project (SKP) pipelines. Direction-independent and direction-dependent calibration and imaging were performed using PREFACTOR (van Weeren et al. 2016; Williams et al. 2016; de Gasperin et al. 2019) and the ddf-pipeline, which includes DDFACET (Tasse et al. 2018) and KILLMS (Tasse 2014a,b; Smirnov & Tasse 2015). The quality towards the targets was improved by Botteon et al. (2022) using the extraction and self-calibration procedure described in van Weeren et al. (2021). We re-imaged the extracted and self-calibrated data instead of using the images from Botteon et al. (2022) to perform a tailored subtraction of discrete sources corresponding to our clusters. The source-subtracted images in Botteon et al. (2022) were produced with an inner uv-cut of 80λ to eliminate large-scale Galactic emission ($\sim 40'$), while here we applied a higher inner uv-cut of 200λ (corresponding to physical scales of 3.6 Mpc for A773 and 4.5 Mpc for A1351) during imaging, matching the shortest baseline of the uGMRT, to ensure consistency between the images at both frequencies. Imaging was performed using WSCLEAN v3.6 (Offringa et al. 2014) with Briggs weighting (Briggs 1995) using a robust parameter of -0.5 and applying different uv -tapers to produce images at varying resolutions. The multi-scale, multi-frequency deconvolution algorithm (Offringa & Smirnov 2017) was enabled and the bandwidth was divided into six frequency channels per imaging run. The systematic uncertainties due to flux density scale calibration is set to 10% for LoTSS-DR2 (Shimwell et al. 2022).

2.2. uGMRT observations

Both clusters were observed with the uGMRT in GMRT Software Backend (GSB) and GMRT Wideband Backend (GWB) Band 4. GSB has a central frequency of 610 MHz with a bandwidth of 32 MHz subdivided into 256 channels. For GWB, the central frequency was 650 MHz, observed with a bandwidth of 200 MHz split into 2048 channels. Both GSB and GWB had an integration time of 4s and measured only total intensity. (Project code: 43_023, P.I. R.Cassano). Each cluster was observed in 6 hr parallel in GSB and GWB. 3C48 was used as the primary calibrator for the processing of A773, and 3C386 was used for A1351. Data were processed using Source Peeling and Atmospheric Modeling (SPAM Intema et al. 2009). Using the final GSB images, a source catalog was generated with Python Blob Detector and Source Finder (PyBDSF Mohan & Rafferty 2015) to model the sky and perform direction-dependent calibration on GWB. GWB data were split into four 50 MHz sub-bands for calibration. Finally, the calibrated sub-bands were imaged

¹ Both clusters belong to the sample of PSZ2 clusters detected in the LoTSS-DR2 (LoTSS-DR2/PSZ2).

Table 1: Galaxy cluster properties.

Properties	PSZ2 G166.09+43.38 (A773)	PSZ2 G139.18+56.37 (A1351)
Optical Richness	Optically rich, Abell class 2 ^(a)	Optically rich, Abell class 2 ^(a)
Redshift (z)	0.217	0.322
M_{500} (M_{\odot})	$6.85 \times 10^{14(d)}$	$6.87 \times 10^{14(d)}$
X-ray Luminosity (L_X)	$12.5 \times 10^{44} h_{50}^{-2}$ erg s $^{-1(e)}$	$8.4 \times 10^{44} h_{50}^{-2}$ erg s $^{-1(f)}$
ICM Temperature (T_X)	7–9 keV ^(g)	~ 9 keV ^(c)
Concentration parameter (c)	$1.84 \times 10^{-1} \pm 6.80 \times 10^{-3(h)}$	$8.6 \times 10^{-1} \pm 5.9 \times 10^{-3(h)}$
Centroid shift (w)	$1.83 \times 10^{-1} \pm 5.71 \times 10^{-3(h)}$	$4.7 \times 10^{-1} \pm 8.49 \times 10^{-3(h)}$

Notes. ^(a) Dahle et al. (2002); Abell et al. (1989). , ^(b) Barrena et al. (2007). , ^(c) Barrena et al. (2014). , ^(d) Planck Collaboration XXVII (2016). , ^(e) Ebeling et al. (1996). , ^(f) Allen et al. (2003); Böhringer et al. (2000). , ^(g) Rizza et al. (1998); Govoni et al. (2004); Ota & Mitsuda (2004), ^(h) Botteon et al. (2022); Zhang et al. (2023).

using the same procedure as that of LOFAR imaging except that the bandwidth was divided into four frequency channels per imaging run (i.e, 50MHz per channel). Similar to LOFAR imaging, an inner uv -cut of 200λ was applied to the images. The systematic uncertainties due to flux scale calibration are set to 5% for the observations in Band 4 (Chandra et al. 2004).

2.3. Integrated synchrotron spectra and source subtraction

To optimize the analysis of diffuse emission, images were generated using various gaussian tapers to increase the weighting of shorter baselines for both LOFAR and uGMRT (see Table. 2). The noise levels of the high-resolution and low-resolution images of LOFAR and uGMRT are reported in Table 2. Since the focus of this study is the radio halo emission, compact sources or contaminants within or near the halo emission were subtracted out. Initially, we created a high-resolution image containing only the compact sources with a Briggs parameter of -0.5 and a uv -cut corresponding to a physical scale of 250 kpc (consistent with Botteon et al. (2022)) at the cluster redshift (A773 - 2893 λ , A1351 - 3892 λ) to remove their contribution from large scale diffuse emissions. The model visibilities of the discrete sources were obtained from WS CLEAN -predict function and they were subtracted from the original data. The subtracted visibilities were subsequently imaged enabling the -multi-scale de-convolution algorithm for different taper values (5'', 10'', 15'' and 20''). A mask was generated from this image by selecting clean components above a 3σ (σ is the rms noise of the image) threshold and then applied in a final imaging run using -fits-mask and with an inner uvcut of 200λ . Following it, the LOFAR and uGMRT images were convolved to a common resolution using CASA to enable a consistent comparative analysis. The image in which maximum extended emission was recovered ($50'' \times 50''$ for A773 and $33'' \times 33''$ for A1351 Fig. 3, 4) without compromising the image fidelity was used to find the flux density of the halos. To test the consistency of this source subtraction process, we compared the flux density obtained from the source-subtracted images with that derived by algebraically subtracting the flux densities of the discrete sources from the total flux of the halo (including discrete sources). The results were consistent within 1σ uncertainty for both the LOFAR and uGMRT images.

2.4. Flux density and spectral index measurement

To measure the flux density of the radio halo in LOFAR and uGMRT images, we adopted two methods which are explained in the next section.

2.4.1. 2σ contours

In the first method, we integrated the flux density within the region defined by the 2σ contours of the radio halo. To assess consistency and potential differences in the emission size between LOFAR and uGMRT, we used two regions: one defined by the LOFAR 2σ contours and the other by the uGMRT 2σ contours. For each of these regions, we measured the integrated flux density in both the LOFAR and uGMRT images and derived the corresponding spectral slope. The uncertainty in the flux density was calculated by the following formula,

$$\Delta S_{\nu} = \sqrt{(fS_{\nu})^2 + N_{\text{beam}}\sigma_{\text{rms}}^2 + \sigma_{\text{sub}}^2}, \quad (1)$$

where f represents the systematic uncertainties due to absolute flux scale errors (see Sec. 2.1, 2.2). σ_{rms} is the map noise level, N_{beam} is the number of beams covering the halo region, and σ_{sub} is the uncertainty of the source subtraction in the uv -plane which was calculated by following the procedure described in Botteon et al. (2022). The flux density values are listed in the Table 3. From the measured flux densities, we determined the spectral index α and its error. The error in the α was determined by

$$\Delta\alpha = \frac{1}{\ln \frac{\nu_1}{\nu_2}} \sqrt{\left(\frac{\Delta S_1}{S_1}\right)^2 + \left(\frac{\Delta S_2}{S_2}\right)^2}. \quad (2)$$

2.4.2. LOFAR model injection

Injection of an exponential model has been the most widely employed technique to estimate upper limits in cases of radio halo non-detection, often caused by missing short baselines or poor sensitivity (Brunetti et al. 2007; Venturi et al. 2008; Kale et al. 2013; Bruno et al. 2023). As a step forward to this approach, we adopt a method with a key improvement of using a realistic model: using LOFAR model obtained during the LOFAR imaging process, rather than an idealized exponential profile to inject into the uGMRT visibilities. A similar strategy was employed by Giacintucci et al. (2014), who injected the CLEAN components of a mini-halo observed with the GMRT at 617 MHz into Very

Cluster name	Central frequency [MHz]	Resolution ['' \times '']	Beam position angle [deg]	uv min [λ]	uv-taper [']	σ_{rms} [$\mu\text{Jy beam}^{-1}$]
PSZ2 G166.09+43.38 (A773)	144	7.9 \times 4.6	92.3	200	—	76.0
	144	34.2 \times 31.6	7.9	200	28.4	203.9
	650	8.8 \times 2.9	75.5	200	—	16.3
	650	31.6 \times 16.6	54.7	200	20	37.7
PSZ2 G139.18+56.37 (A1351)	144	8.6 \times 4.3	97.8	200	—	67.2
	144	28.0 \times 24.1	30.2	200	21.3	163.3
	650	4.6 \times 3.3	150.1	200	—	12.5
	650	23.8 \times 17.8	173.2	200	20	57.4

Table 2: Image properties of the clusters A773 & A1351.

Large Array (VLA) data at 4.86 GHz and 8.44 GHz for different spectral indices. This method not only provides robust upper limits, but also allows us to quantify the flux density loss attributed due to instrumental limitations. It offers us a more realistic estimate of the halo flux and the spectral index and an opportunity to check for possible systematics in the spectral index estimate.

The following steps briefly describe the injection method:

We begin the analysis by assuming a flux density to be injected into the uGMRT visibilities. The LOFAR model image is then rescaled to this flux density by adopting the spectral index α required to reproduce the corresponding value at 650 MHz. The rescaling is applied to the CLEAN components associated with the radio halo in the LOFAR low-resolution model, using an inner *uv*-cut of 80λ , to include all recoverable diffuse emission by LOFAR. The offset to inject the radio halo is chosen to be close enough to the center to avoid significant primary beam attenuation, while ensuring that the region is free of contaminating sources or imaging artifacts (see Fig. A.1). After the injection, the "updated" uGMRT dataset is imaged following the standard procedure (see Sect. 2.2, Sect. 2.3), and the recovered flux density of the injected halo is measured within the 2σ contour of the new image. To account for local noise fluctuations and potential contributions from discrete sources, the flux density measured in the same region prior to injection is subtracted from the recovered flux. If the recovered flux density lies within $\pm 5\%$ of the flux density measured in the observations within 2σ contours, the corresponding injected flux density is considered a reliable estimate of the halo's flux density. Consequently, the spectral index α used to obtain this injected flux is regarded as the reliable spectral index of the halo. This value should be considered a lower limit on α , as it assumes no flux density loss in LOFAR. Bruno et al. (2023) (see their fig. 14) showed that flux density losses in LOFAR observations are $\leq 10\%$ for radio halos with diameters between 7.5' and 10.5'. However, over the broad frequency range of 144–650 MHz, such flux density losses have a negligible impact on the spectral index α . Since the halos considered in this study have maximum sizes of $\sim 10'$, LOFAR flux density losses are expected to be minimal, and the model images are deemed suitable for injection. The procedure is then repeated iteratively using different values of injection fluxes until the recovered flux matches the observed flux.

If the spectral slope derived from observations between the LOFAR and uGMRT images is steeper than the slope obtained by the injection method, it indicates that the uGMRT has suffered losses due to missing baselines and sensitivity issues.

3. Results

High-resolution LOFAR and uGMRT images of A773 are reported in Fig. 1. The central regions of the cluster show the presence of multiple radio sources. At the resolution of 10'', the radio halo detected in LOFAR is larger in size than uGMRT (Fig 1, left panel).

High-resolution images of A1351 (see Fig. 2) show a more complex radio morphology which include different sources, including one of the two brightest cluster galaxies (BCG), a tailed galaxy (TG), and an extended region of diffuse emission referred to as the "ridge" (Fig. 2). In the LOFAR high-resolution image, we reached a resolution of 8.64'' \times 4.32''. However, at this resolution, TG and the ridge are still not resolved. The improved sensitivity and high angular resolution of the uGMRT image (4.68'' \times 3.34''), clearly reveals both the TG and the ridge structure. Notably, the morphological details of the ridge are distinctly resolved. The ridge extends for a projected length of ~ 470 kpc and is located at a projected distance of ~ 500 kpc from the center of the cluster. The cluster center was set at the location of BCG, as described in Barrena et al. (2014). From the head of the TG, the center of the ridge is ~ 330 kpc away.

3.1. Radio halo

3.1.1. A773

The RH in A773 is bright and extended, clearly detected in both LOFAR and uGMRT images, and it is located at the center of the cluster, following the X-ray emission (Fig. 3). The halo extends over a largest linear size (LLS) of ~ 2 Mpc and is elongated along NE-SW direction in both LOFAR and uGMRT images aligning with the previous studies (Govoni et al. 2001b; Barrena et al. 2007). The integrated flux density values of the halo in LOFAR and uGMRT, based on the LOFAR 2σ contour region, are 143.4 ± 14.5 mJy and 27.1 ± 1.5 mJy, respectively. When measured using the uGMRT 2σ contour regions, the integrated flux density values are 141.1 ± 14.3 mJy and 26.5 ± 1.5 mJy in LOFAR and uGMRT respectively. The integrated spectral index α obtained in the two cases are consistent -1.10 ± 0.08 . In applying the injection method (see Sect 2.4.2), the flux density of the injected region measured in LOFAR is 149.2 ± 15.1 mJy. Upon rescaling the model to 650 MHz with an α of -1.1, the flux density obtained was 28.9 mJy. When this rescaled flux was injected into the uGMRT visibilities, a flux density of 25.6 mJy was recovered. This value is consistent within $\pm 5\%$ with the flux density measured within the 2σ contour using both LOFAR and uGMRT methods. Therefore, we can conclude that $\alpha \sim -1.1$ is a reliable estimate of the halo spectral index, and that ~ 28.9 mJy is a likely value for its flux density at 650 MHz, with uGMRT experiencing a flux density loss of approximately $\sim 7\%$. The integrated flux density and spectral index values using different methods are reported in Table. 3.

3.1.2. A1351

For A1351, the process of source subtraction was challenging due to the presence of many contaminating sources that needed to be removed to isolate the diffuse radio halo emission. Since the BCG, TG, and the ridge could still leave some residuals after

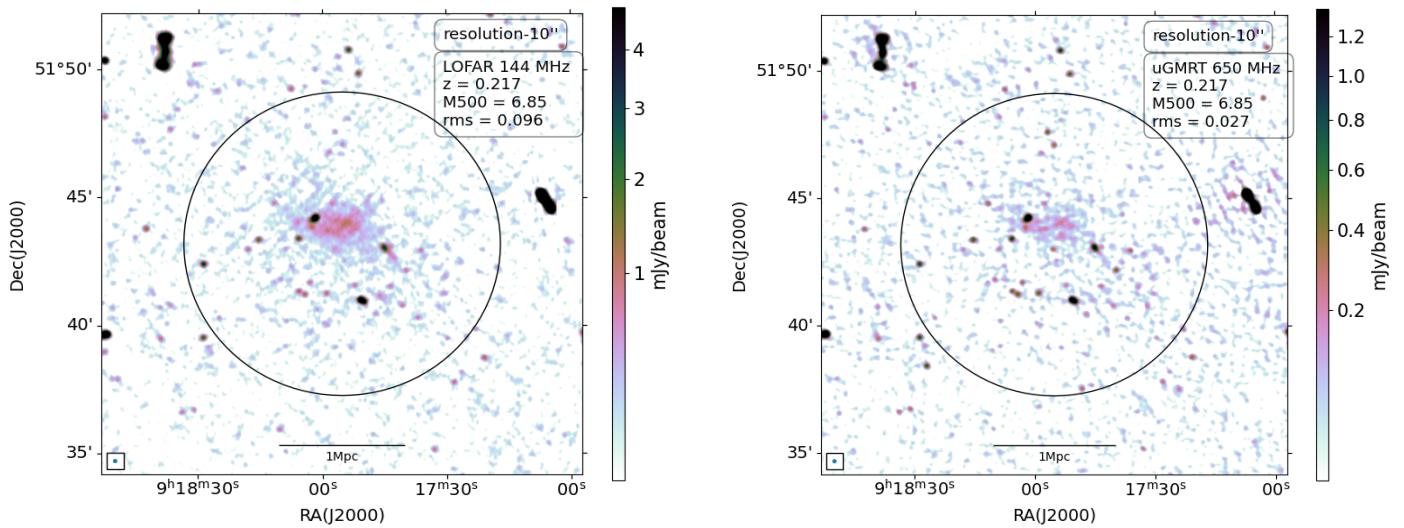


Fig. 1: *Left:* High resolution LOFAR image of A773 at 144 MHz. *Right:* High resolution uGMRT image of A773 at 650 MHz. Both images are at a resolution of $10'' \times 10''$, with M_{500} in units of $10^{14} M_{\odot}$ and rms in mJy/beam. The drawn region represents the r_{500} scale of the cluster.

subtraction they were masked during the subtraction of discrete sources while the other contaminants were removed. The radio halo in A1351 is large, bright, and extended, and is clearly detected in both LOFAR and uGMRT observations. Its morphology broadly follows the distribution of the X-ray emission (Fig. 4) with diffuse emission extending up to r_{500} . However, the faint emission detected near and beyond r_{500} in the NE region in both the LOFAR and uGMRT images (regions A & B in Fig 4) remains of uncertain origin. Higher sensitivity observations are necessary to discriminate the possible contribution of discrete sources or residuals in the images. High-resolution images from LOFAR hint at the presence of a faint radio galaxy causing this emission (region A Fig 4), although its location at the outskirts of the cluster raises the possibility that it could also be a relic. This region lacks significant X-ray emission and does not show any optical counterpart in Panoramic Survey Telescope & Rapid Response System (Pan-STARRS; (Chambers et al. 2016)) observation. Therefore, the size and flux density of the radio halo were measured excluding this faint emission. The halo has a LLS of ~ 2.0 Mpc in both LOFAR and uGMRT. If the faint emission near and beyond r_{500} is included as part of the halo, the total extend of the diffuse emission increases to ~ 2.6 Mpc in both the LOFAR and uGMRT images.

The integrated flux density values of the halo in LOFAR and uGMRT using the different methods outlined in Sect. 2.4.1 are reported in Table. 3. In both cases, the integrated spectral index is -0.95 ± 0.07 . The flux density contributed only by the ridge to the halo is 95.5 ± 9.5 mJy in LOFAR and 21.7 ± 1.1 mJy in uGMRT. When all the contaminants (BCG, tail, and ridge) are taken into account, the total contribution to the halo flux increases to 121.4 ± 12.1 mJy and 29.5 ± 1.4 mJy in LOFAR and uGMRT, respectively. The uGMRT flux density measurement aligns (within 1σ uncertainty) with the flux density reported by Chatterjee et al. (2022), which is 87.2 ± 6.1 mJy (within 3σ contours) using GMRT at 610 MHz. In applying the injection method (see Sect 2.4.2), the flux density of the injected model measured by LOFAR is 408.6 ± 40.9 mJy. Rescaling the model to 650 MHz with $\alpha = -0.95$, the flux density obtained was 97.6 mJy. When this rescaled flux was injected into the uGMRT vis-

ibilities, a flux density of 88.0 mJy was recovered. This value is within $\pm 5\%$ of the flux density value measured within the 2σ contour using both LOFAR and uGMRT methods. Therefore, we can argue that $\alpha \sim -0.95$ is a reliable measurement for the radio halo spectral index and 97.6 mJy is a reliable measurement of the flux density of the halo at 650 MHz, with uGMRT experiencing a flux density loss of 4-7%.

3.2. Spectral index map

Spectral index (SI) maps between LOFAR 144 MHz and uGMRT 650 MHz source-subtracted images were generated applying a common inner uv -cut of 200λ to sample the same spatial scales and masking regions below 3σ threshold. The images were convolved to a common resolution, regridded, and aligned. Regridding was performed using CASA, while image alignment was carried out using BROADBAND RADIO ASTRONOMY TOOLS (BRATS), (Harwood et al. 2020) Image Aligner². The spectral index map of the aligned images was produced using CASA and does not account for flux density losses in uGMRT identified through the real LOFAR model injection. These losses primarily affect the faint, diffuse emission located in the peripheral regions; however, they are on the order of a few percent, as shown in Sec. 3.1.1 and 3.1.2, and therefore do not significantly impact the spectral analysis.

3.2.1. A773

For A773 the resulting SI map reveals a spatial variation of the spectral index with values ranging between -1.4 and -0.6 (Fig 5). To further illustrate this variation, the spectral index measured within radio beam sized grids in the SI map is presented as a histogram (Fig. B.1). In the core of the cluster the spectral index remains constant around -1.0. In the south-east edge of the map, the region that falls inside 6σ contour shows spectral flattening, and this is attributed to the source subtraction residuals which becomes prominent at low resolution. This region also exhibits

² <https://github.com/JeremyHarwood/bratsimagealignment>

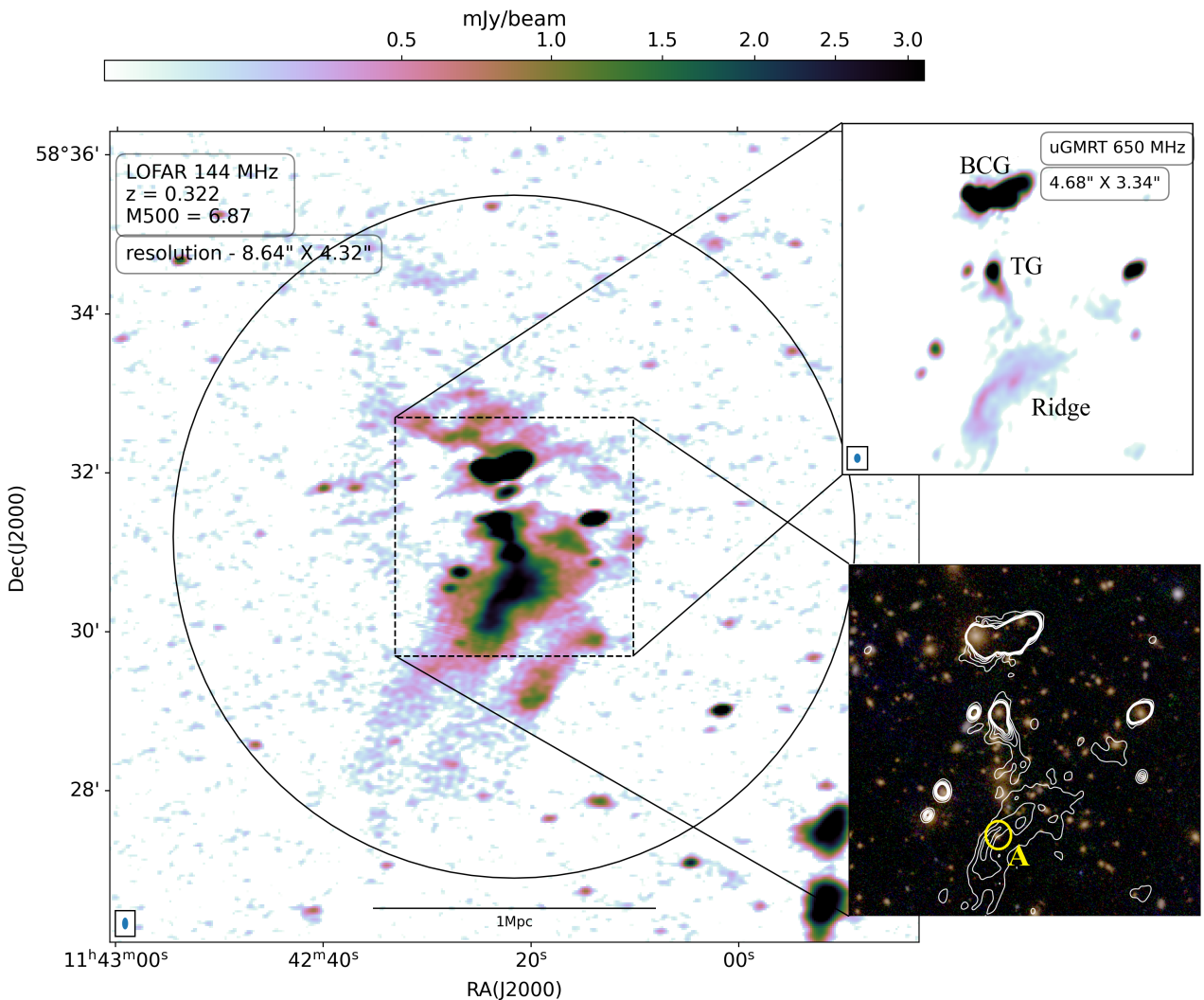


Fig. 2: High-resolution LOFAR image of A1351 at 144 MHz with a resolution of $8.64'' \times 4.32''$ and an rms noise of $68 \mu\text{Jy beam}^{-1}$. The black circle represents the r_{500} scale of the cluster. Inset top: Zoom-in of the cluster center at uGMRT 650 MHz at a resolution of $4.68'' \times 3.34''$. The rms of the uGMRT image is $13 \mu\text{Jy beam}^{-1}$. Inset bottom: Optical Pan-STARRS (g,r,i) image of the cluster center overlaid with uGMRT radio contours at levels of $(9, 18, 27, 36, 45, 52) \times \sigma_{rms}$. M_{500} is given in units of $10^{14} M_{\odot}$.

Cluster name	Resolution	Flux density LOFAR (mJy)	Flux density uGMRT (mJy)	Spectral index values
A773	$50'' \times 50''$	143.4 ± 14.5	27.1 ± 1.5	-1.10 ± 0.08
	$50'' \times 50''$	141.1 ± 14.3	26.5 ± 1.5	-1.10 ± 0.08
	—	149.2 ± 15.1	28.9	-1.10 ± 0.07
A1351	$33'' \times 33''$	392.6 ± 39.3	93.4 ± 4.7	-0.95 ± 0.07
	$33'' \times 33''$	385.2 ± 38.5	91.5 ± 4.6	-0.95 ± 0.07
	—	408.6 ± 40.9	97.6	-0.95 ± 0.07

Table 3: Flux density and spectral index values for clusters A773 and A1351 using various methods, presented in the order of LOFAR 2σ contours, uGMRT 2σ contours and LOFAR model injection (For clarification on the methods and flux density values, see sec 3.1.1 and 3.1.2).

high spectral index error values, making the spectral index less reliable than in the other regions (see Fig 5).

3.2.2. A1351

For A1351, SI maps were generated for both high-resolution and low-resolution radio images. The high-resolution SI map ($7'' \times 7''$) is important for studying the impact of ridge and

other radio features on the halo. To create the high-resolution images, we used a Briggs weighting parameter of -1 , with no taper and an inner uv -cut of 200λ , for both LOFAR and uGMRT datasets. The SI map was then produced following the procedure described earlier (see Fig. 6). From the high-resolution spectral index map, we observe a steepening of the spectral slope along the tail of the TG (Fig. 6). On the other hand, the ridge, does not show any significant spectral gradient; its spectral index is

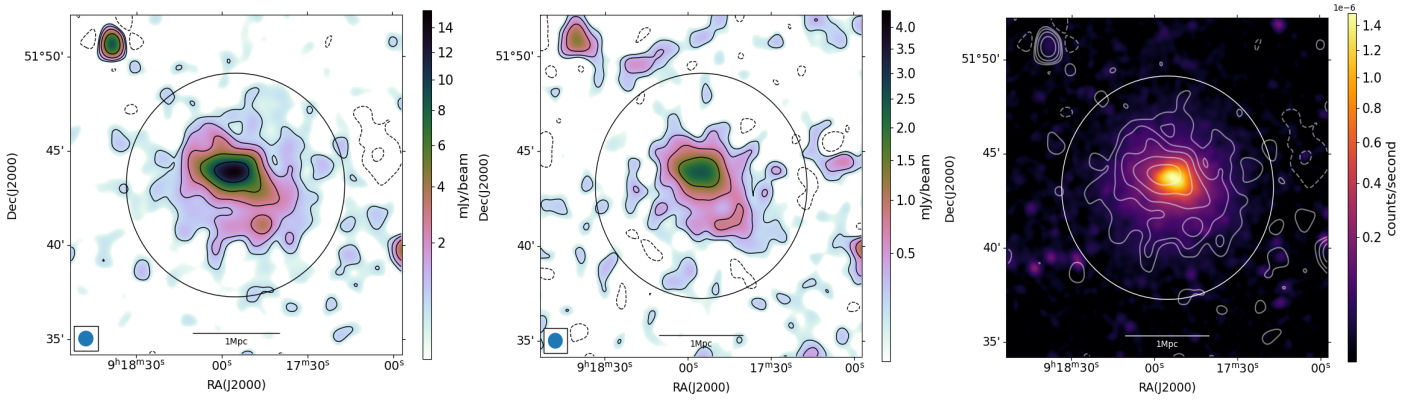


Fig. 3: *Left*: Low resolution source subtracted LOFAR image of A773 at 144 MHz overlaid with LOFAR 2σ contours. *Middle*: Low resolution source subtracted uGMRT image of A773 at 650 MHz overlaid with uGMRT 2σ contours. *Right*: XMM image of A773 overlaid with LOFAR source subtracted contours. The contour levels are spaced as $(-2, 2, 4, 8, 16, 32) \times \sigma_{rms}$. LOFAR and uGMRT source subtracted images have a resolution of $50'' \times 50''$. The region drawn around the halo represents the r_{500} scale of the cluster.

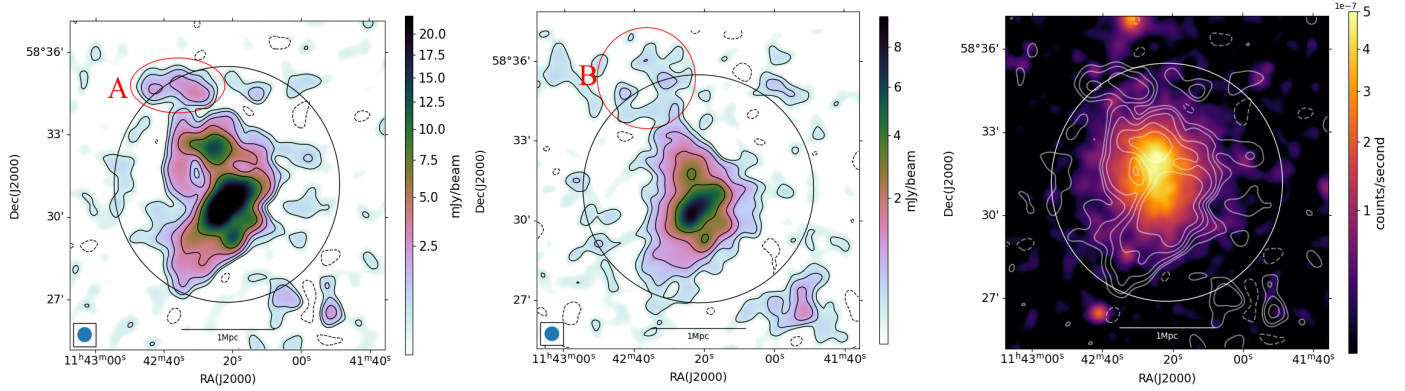


Fig. 4: *Left*: Low resolution source subtracted LOFAR image of A1351 at 144 MHz overlaid with LOFAR 2σ contours. *Middle*: Low resolution source subtracted uGMRT image of A1351 at 650 MHz overlaid with uGMRT 2σ contours. *Right*: XMM image of A1351 overlaid with LOFAR source subtracted contours. The contour levels are spaced as $(-2, 2, 4, 8, 16, 32) \times \sigma_{rms}$. LOFAR and uGMRT source subtracted images have a resolution of $33'' \times 33''$. The region drawn around the halo represents the r_{500} scale of the cluster.

~ -0.9 . A previous study by Chatterjee et al. (2022), based on an SI map between GMRT and VLA (610 MHz - 1.4 GHz), reported a spectral steepening across the ridge, suggesting the presence of a shock downstream. However, in our SI map, no clear gradient is detected across the ridge.

For the low-resolution, source-subtracted spectral index map of A1351 (Fig. 7), we adopted a different approach compared to the method used for A773. Specifically, the BCG, TG, and the ridge, were not subtracted before producing the SI maps (Fig. 7). The other contaminating sources were removed. This was done intentionally because they are challenging to remove and there could be some residuals of the bright tails even after subtraction. This will also allow us to investigate whether any spectral gradient exists that could suggest a connection to a shock or support the interpretation of the ridge as a radio relic. Spectral flattening is observed in the regions of TG and BCG (Fig. 7) but the image does not provide significant information regarding particle acceleration processes.

3.3. Point-to-Point analysis

To investigate the connection between the thermal and non-thermal components in these galaxy clusters we performed a point-to-point analysis of their radio and X-ray surface brightness ($I_{\text{Radio}} - I_X$ relation) (Govoni et al. 2001a). Several studies have conducted point-to-point analysis, revealing that clusters with radio halos generally exhibit a positive, sub-linear trend between the radio and X-ray brightness indicating narrower thermal and broader non-thermal components distribution (Giacintucci et al. 2005; Cova et al. 2019; Xie et al. 2020; Hoang et al. 2021; Santra et al. 2024; Balboni et al. 2024). In our paper, point-to-point analysis was conducted using the methodology described in Balboni et al. (2024) where surface brightness was extracted from the radio (I_R) and X-ray (I_X) images by constructing a grid over the regions above the 2σ level. Each box inside the grid has an area equal to the radio beam size, ensuring that the measurements remain independent (see Fig. C.1).

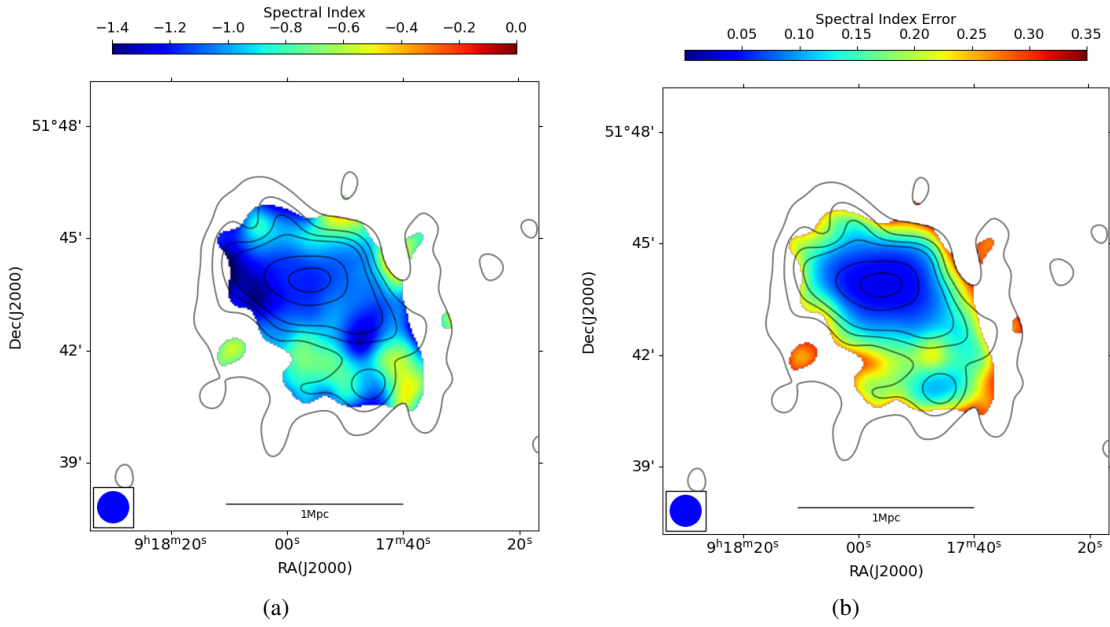


Fig. 5: *From left:* Spectral index map between the source-subtracted images of LOFAR at 144 MHz and uGMRT at 650 MHz of A773 and its error map, with a resolution of $50'' \times 50''$, overlaid with 3 sigma contours of the LOFAR image. The contour levels for LOFAR are set at $(3, 6, 9, 12, 27, 41) \times \sigma_{\text{rms}}$, where σ_{rms} is 0.30 mJy/beam.

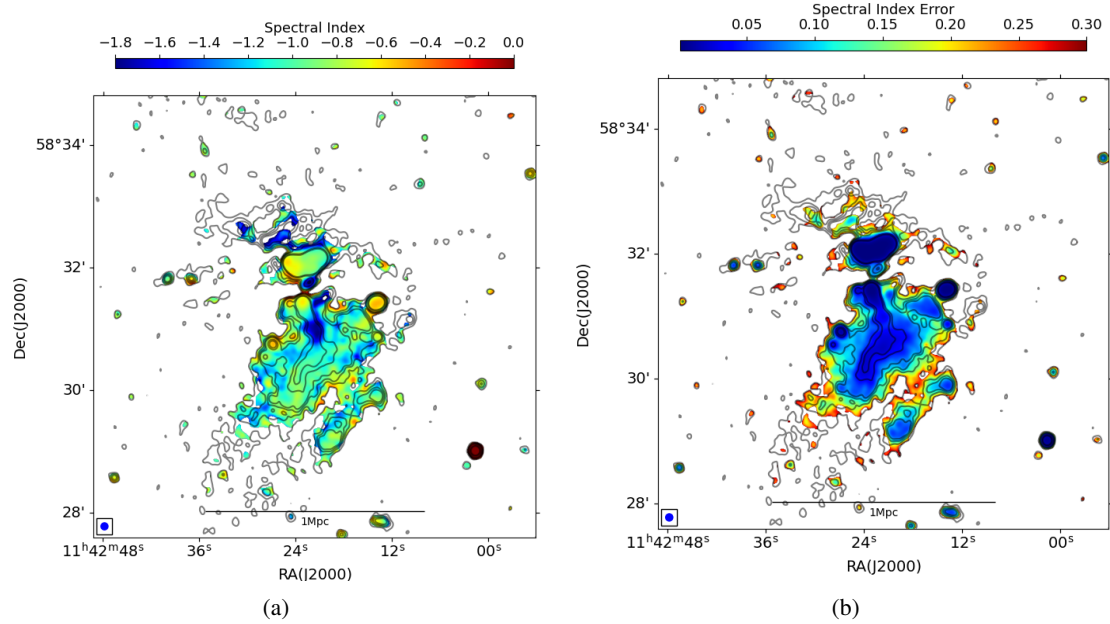


Fig. 6: *From left:* Spectral index map between the high resolution images of LOFAR at 144 MHz and uGMRT at 650 MHz of A1351 and its error map, with a resolution of $7'' \times 7''$, overlaid with 3 sigma contours of the LOFAR image. The contour levels for LOFAR are set at $(3, 6, 9, 12, 27, 41) \times \sigma_{\text{rms}}$, where σ_{rms} is 0.071 mJy/beam.

3.3.1. A773

In the analysis of the A773 cluster, the source-subtracted images from LOFAR and uGMRT were convolved to a common resolution of $50'' \times 50''$. Focusing on regions above the 2σ noise level, these images were compared with the X-ray image obtained from XMM-Newton (Zhang et al. 2023). As depicted in Figure 8, the best-fit relation between radio and X-ray surface brightness yields a slope of 0.81 ± 0.06 for LOFAR-XMM and 0.70 ± 0.06 for uGMRT-XMM. This sublinear correlation aligns

with the expectations from the turbulent re-acceleration model of radio halos (Govoni et al. 2001a; Brunetti & Jones 2014; Balboni et al. 2024). The Pearson correlation coefficient r_p is 0.87 for LOFAR-XMM and 0.88 for uGMRT-XMM, with a scatter σ of 0.35 and 0.29 around the best-fit relation (see Table 4).

3.3.2. A1351

Similar to cluster A773, the source-subtracted images for cluster A1351 from LOFAR and uGMRT were convolved to a com-

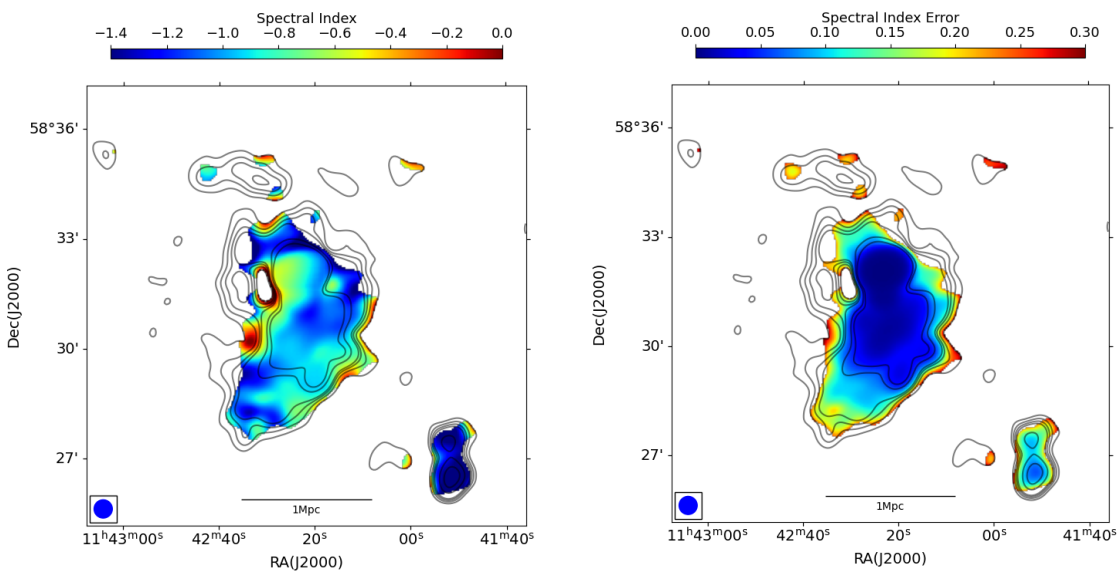


Fig. 7: *From left:* Spectral index map between the source subtracted images of LOFAR at 144 MHz and uGMRT at 650 MHz of A1351 and its error map, with a resolution of $30'' \times 30''$, overlaid with 3 sigma contours of the LOFAR image. The contour levels for LOFAR are set at $(3, 6, 9, 12, 27, 41) \times \sigma_{\text{rms}}$, where σ_{rms} is 0.19 mJy/beam. *Note:* The BCG, TG, and the ridge were not subtracted in the source subtracted LOFAR and uGMRT final images used to generate the spectral index map.

Table 4: Point-to-point analysis of A773 and A1351. r_p denotes the Pearson correlation coefficient with the p-value in brackets. σ represents the scatter around the best-fit relation.

Properties	A773	A1351
Best-fit (LOFAR-XMM)	0.81 ± 0.06	0.98 ± 0.15
Best-fit (uGMRT-XMM)	0.70 ± 0.06	0.93 ± 0.17
r_p (LOFAR-XMM)	0.87 (p=1.4e-22)	0.48 (p=1.2e-5)
r_p (uGMRT-XMM)	0.88 (p=1.0e-17)	0.50 (p=1.4e-5)
σ (LOFAR-XMM)	0.35	0.87
σ (uGMRT-XMM)	0.29	0.85

mon resolution of $33'' \times 33''$. Regions above the 2σ noise level were compared with the X-ray image obtained from XMM-Newton, and their respective surface brightness within the grids (see Fig C.1) were plotted (Fig 8). This analysis yielded a best-fit relation of 0.98 ± 0.15 for LOFAR-XMM, with a Pearson correlation coefficient $r_p \sim 0.48$ and a scatter σ of 0.87. For uGMRT-XMM, the best-fit relation was 0.93 ± 0.17 , with a Pearson correlation coefficient $r_p \sim 0.50$ and a scatter σ of 0.85 (see Table. 4). In both cases, the high value of the scatter might suggest a weak or absent correlation. We decided to investigate which part of the halo contributes more to the scatter, so we divided the RH into two distinct regions: the center and the outer region, fitting them separately. In both the regions, the relations were weakly correlated. A further subdivision of the RH into three spatial regions did not improve the correlation. However, this analysis showed that the scatter primarily arises from regions affected by BCG and the ridge. We did not attempt additional subdivisions due to the limited number of grids available for a reliable fit.

4. Discussion

4.1. A773

A773 is a dynamically disturbed cluster characterized by a bimodal velocity distribution of galaxies. Optical observations from Digitized Sky Survey (DSS) reveal two galaxy substructures with one of them aligning with the center of X-ray emission (Govoni et al. 2004). Significant amount of substructure in A773 was first shown by ROSAT (Rizza et al. 1998; Govoni et al. 2001b; Starck & Pierre 1998). A773 has experienced multiple merger events involving one or two massive galaxy groups. One of the major mergers was along the north-south (N-S) direction, involving the cluster and the group that contained the second dominant galaxy in the system. The most recent merger is along NEE-SWW direction, as traced by the X-ray emission (Barrena et al. 2007). Since the X-ray peaks do not correlate with the spatial distribution of galaxies it indicates an advanced merging phase (Barrena et al. 2007). This was further supported by the position of the dominant galaxies along the N-S direction, while the X-ray emission extending along NEE-SWW direction. Barrena et al. (2007) also expect that the merger axis is close to the line of sight (LOS).

From the source-subtracted images of A773, it is evident that the extent of the diffuse radio emission observed in LOFAR and uGMRT is similar (Fig. 3). Contrary to the findings of Govoni et al. (2004), the radio halo follows the X-ray emission along NEE-SWW direction. The discrepancy may have resulted from the limited sensitivity of the previous radio and X-ray observations. The radio halo exhibits an integrated spectral index of $\alpha_{144}^{650} \sim -1.0$. The SI map (Fig. 5) and the corresponding histogram (Fig. B.1) reveal significant spatial variations in α , suggesting the presence of complex particle acceleration processes within the cluster.

The point-to-point analysis reveals a best-fit sublinear correlation between the radio and X-ray surface brightness distributions in both LOFAR-XMM and uGMRT-XMM dataset (Fig 8). There is some scatter present in both the plots. The level

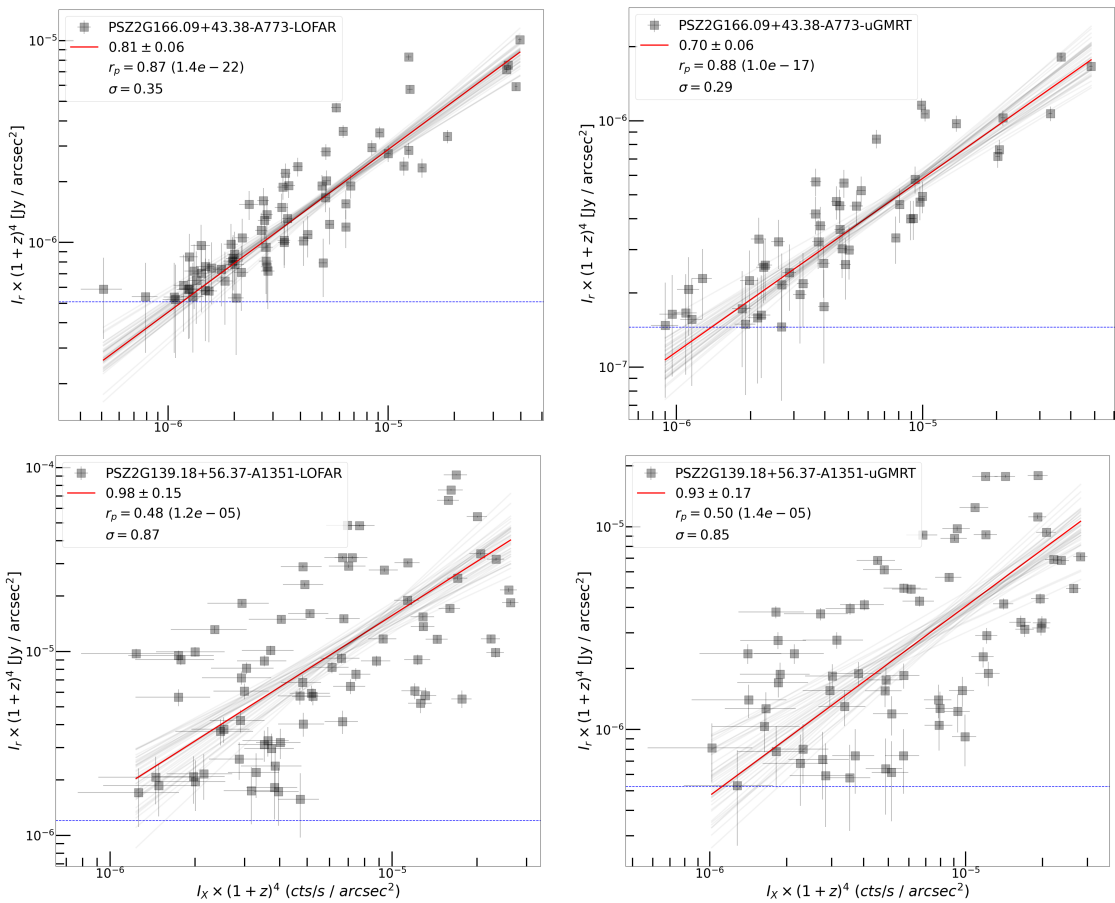


Fig. 8: *Top:* Radio and X-ray surface brightness comparison of LOFAR and uGMRT images at a resolution of $50'' \times 50''$ with X-ray XMM image of A773 within the regions marked by boxes in Fig. C.1. *Bottom:* Same for A1351 at $33'' \times 33''$ resolution. The red line indicates the best-fit, blue dashed line is the 2σ contour threshold. The Pearson correlation coefficient is denoted by r_p with the corresponding p-values (in brackets). σ indicates the scatter around the best-fit relation.

of scatter is negligible and agrees with the average intrinsic scatter reported by [Balboni et al. \(2024\)](#), who investigated the radio–X-ray correlations in five other clusters hosting radio halos. The best-fit relation for LOFAR–XMM is steeper than that for uGMRT–XMM. This difference is likely driven by the flattening of the spectral indices (see Fig. 5) towards the halo outskirts, where the X-ray emission becomes fainter. A possible explanation for the spectral flattening is the presence of particles re-accelerated by merger-driven shocks, likely associated with the recent merger activity along the NE–SW axis. However, we cannot exclude the possibility that additional mechanisms are at work in the cluster.

4.2. A1351

A1351 is also a dynamically disturbed galaxy cluster exhibiting a bimodal velocity distribution with two distinct peaks separated by approximately 2500 km s^{-1} in the rest frame, indicative of an active merger ([Barrena et al. 2014](#)) along the LOS. The X-ray peak coincides with one of the two BCGs, which is also the only one detected in radio (marked as BCG in Fig. 2). Analysis of Chandra X-ray data reveals four substructures along the N–S axis, two of which are associated with the BCGs and are primarily responsible for the observed bimodality in the galaxy velocity distribution. A1351 hosts a giant radio halo that extends along NE–SW with a LLS of $\sim 2 \text{ Mpc}$ in both LOFAR and uGMRT images (Fig 4) and the X-ray surface brightness distribution is

elongated along N–NE to S–SW axis. The halo is asymmetrical with respect to X-ray emission, consistent with previous studies ([Giacintucci et al. 2009](#); [Giovannini et al. 2009](#); [Chatterjee et al. 2022](#); [Botteon et al. 2022](#)). The presence of numerous discrete radio sources at the cluster center complicates the analysis of the radio halo, as it significantly hinders accurate source subtraction and the study of the diffuse emission. An important feature within this galaxy cluster is the ridge, see Fig. 2. The ridge is claimed to be a radio relic in earlier research of [Chatterjee et al. \(2022\)](#); [Giacintucci et al. \(2009\)](#) and [Barrena et al. \(2014\)](#); but high-sensitivity and high-resolution imaging with uGMRT at 650 MHz (Figure 2) suggests an atypical morphology. Analysis of Chandra X-ray data by [Chatterjee et al. \(2022\)](#) revealed a surface brightness discontinuity and a temperature jump, indicating a shock propagating along the SW direction. The shock Mach number derived from radio observations and the temperature jump was found to be ≥ 1.5 . It was proposed that since the cluster merger is along the NNE–SSW axis, an axial shock could form the relic ([Chatterjee et al. 2022](#)). According to [Barrena et al. \(2014\)](#), since the ridge is situated at the external boundary of the southernmost X-ray clumps, it suggests that it could be a relic associated with a minor merger along the N–S direction. Despite previous X-ray studies favoring the interpretation of the relic, our analysis raises questions about this classification. The ridge’s morphology (Fig 2), lack of a spectral gradient (Figs 6), and the presence of an optical counterpart in its central region

(Figs. 2) suggest that it is most likely a radio galaxy rather than a projected relic. Furthermore, the tail of the TG interacts with the head of the ridge, supplying relativistic electrons to the ridge and also to the surrounding turbulent medium, where they can be re-accelerated along with electrons from other radio sources within the cluster.

Another unique radio feature observed in A1351 is the extended emission near r_{500} (Fig 4, marked as region A). This region was excluded from the calculations of the size and flux density of the radio halo because of uncertain origin. This region lacks any optical or X-ray counterparts. In their analysis using the VLA, Giacintucci et al. (2009) (refer to their fig. 2) suggested the possibility of a small radio filament close to the extended emission observed near r_{500} . Instead, it could potentially be associated with a radio galaxy or a relic. This is further supported by the findings of Barrena et al. (2014), who dismissed the filament hypothesis due to the absence of X-ray emission or an optical subcluster in that region. Additionally, the uGMRT image at low resolution (Fig. 4, region marked B) shows a morphology that deviates from the LOFAR detection. Due to the morphological differences, a direct comparison between the LOFAR and uGMRT image was also not feasible.

The ridge contributes approximately one-third of the total flux density measured for the RH in LOFAR and uGMRT. The RH in A1351 has an integrated flat spectral index of $\alpha_{144}^{650} \sim -0.95 \pm 0.07$. The low-resolution spectral index map shows no significant spectral index gradient (Fig 7). Our results differ significantly from those reported by Chatterjee et al. (2022) at higher frequency, who found a steeper integrated index of $\alpha = -1.72 \pm 0.33$ for the halo and $\alpha = -1.63 \pm 0.33$ for the ridge between GMRT 610 MHz and VLA 1.4 GHz. The difference in the spectral index could arise from several factors. Our analysis is based on GMRT wide band data (LOFAR-uGMRT), whereas their study used GMRT narrow band observations (GMRT-VLA), offering improved bandwidth coverage and sensitivity in our case. There are also differences in source subtraction methods, the specific regions selected for flux and spectral index measurements, and the possibility of spectral steepening at frequencies higher than 600 MHz.

A1351 is a notable cluster as it hosts a giant radio halo but deviates from the expected sublinear point-to-point correlation. The comparison between LOFAR-XMM and uGMRT-XMM surface brightness shows significant high scatter, which leads to doubts about the existence of a correlation. The observed correlation and scatter is likely influenced by the central contaminants which are not a part of the halo but which might hide a flatter (sub-linear) correlation. This raises the possibility that not all the observed diffuse emission is part of the halo; rather, we may be detecting only a fraction of the halo, with the rest of the emission potentially arising from other sources.

For both clusters, the LOFAR model injection technique was employed to determine the flux density loss of the halos in the uGMRT data-sets. This approach is a step forward from the conventional method of injecting an exponential model to find the upper limits. This method can determine the upper limits in the absence of a radio halo or quantify the flux density loss if a radio halo has been detected by the telescope. For both A773 and A1351, the flux density loss in the uGMRT data-sets ranges between 4% and 7%. Assessing flux density loss is crucial, as losses above 20–30% could bias the results, producing a steeper spectral slope or underestimating the flux density. However, in our analysis, the spectral index slopes obtained from both the methods agree within a 1σ uncertainty.

Accurate measurements of the spectral slope and radio flux density are essential for understanding the origin of radio halos. In the turbulent re-acceleration model, α depends on cluster mass, dynamical state of the merging system, and the mass of any accreted group or cluster (Cassano et al. 2023), providing insights into the physical mechanisms driving halo formation.

Both A773 and A1351 are massive clusters hosting giant radio halos with integrated $\alpha_{144}^{650} \sim -1.0$. A773 shows signs of past mergers, including a recent core passage, while A1351 is undergoing an active merger. These dynamical states likely generate sufficient turbulent energy to power bright halos observable at high frequencies (e.g., 650 MHz). In addition, the presence of numerous radio galaxies around the halos may also supply seed cosmic-ray electrons for turbulent re-acceleration (Vazza & Botteon 2024).

5. Conclusion

Our analysis on the radio halos in A773 and A1351 using LOFAR-uGMRT data allowed to derive the following results:

- The galaxy clusters A773 and A1351 are massive merging clusters both hosting giant radio halos. The LLS of the radio halo in A773 and A1351 is ~ 2 Mpc in both LOFAR and uGMRT images.
- Both A773 and A1351 host numerous radio sources within the halo region. Notably, A1351 contains three significant sources that affect the halo emission: BCG, TG and a ridge. The ridge was considered a relic in Chatterjee et al. (2022); Giacintucci et al. (2009) and Barrena et al. (2014). However, our high-sensitivity and high-resolution images from uGMRT at 650 MHz (Fig 2) raise a question about the nature of this emission as its morphology resembles that of a radio galaxy.
- The flux densities and spectral indices were derived using two approaches: measuring flux densities within 2σ contours in LOFAR and uGMRT images, and modeling with injection of real LOFAR data. Both clusters show an integrated flat spectral index of ~ -1.0 , consistent with both the methods.
- A773 shows varying spectral index in the SI map with no clear trend. A1351 shows no significant spectral gradients in the SI map. Additionally, the ridge in A1351 did not display any spectral gradient, which is in contrast with previous studies (Chatterjee et al. 2022).
- A point-to-point analysis revealed that A773 exhibits a sub-linear relation between radio and X-ray surface brightness in both LOFAR and uGMRT data, which is consistent with expectations of the turbulent re-acceleration scenario (Brunetti & Jones 2014). In contrast, A1351 exhibits a weak or absent correlation between LOFAR-XMM and uGMRT-XMM, with an high scatter ($\sigma \sim 0.85-0.87$) dominating the relationship. We suggest that the presence of numerous contaminants (discrete and diffuse sources embedded within the halo) may obscure the underlying sublinear relation.

As a future work, conducting a LOFAR Very Long Baseline Interferometry (VLBI) and polarization analysis on A1351 could provide further insights into the nature of the ridge and accurate source subtraction.

Acknowledgements. ABon and MBal acknowledges support from the Horizon Europe ERC CoG project BELOVED, GA n. 101169773. FdG and CG acknowledge support from the ERC Consolidator Grant ULU 101086378. SC acknowledges the support from Rhodes University and the National Research Foundation (NRF), South Africa. R.C. and K.S. acknowledges financial support from the INAF grant 2023 “Testing the origin of giant radio halos with joint LOFAR-uGMRT observations” (1.05.23.05.11). Part of The research activities described

in this paper were carried out with contribution of the Next Generation EU funds within the National Recovery and Resilience Plan (PNRR), Mission 4 - Education and Research, Component 2 - From Research to Business (M4C2), Investment Line 3.1 - Strengthening and creation of Research Infrastructures, Project IR0000034 - "STILES - Strengthening the Italian Leadership in ELT and SKA". R.K. acknowledges the support of the Department of Atomic Energy, Government of India, under project no. 12-R&D-TFR-5.02-0700. This paper is based on data obtained with the Giant Metrewave Radio Telescope (GMRT). We thank the staff of the GMRT that made these observations possible. GMRT is run by the National Centre for Radio Astrophysics of the Tata Institute of Fundamental Research. The National Radio Astronomy Observatory is a facility of the National Science Foundation operated under cooperative agreement by Associated Universities, Inc. LOFAR (van Haarlem et al. 2013) is the LOw Frequency ARray designed and constructed by ASTRON. It has observing, data processing, and data storage facilities in several countries, which are owned by various parties (each with their own funding sources), and are collectively operated by the ILT foundation under a joint scientific policy. The ILT resources have benefitted from the following recent major funding sources: CNRS-INSU, Observatoire de Paris and Université d'Orléans, France; BMBF, MIWF-NRW, MPG, Germany; Science Foundation Ireland (SFI), Department of Business, Enterprise and Innovation (DBEI), Ireland; NWO, The Netherlands; The Science and Technology Facilities Council, UK; Ministry of Science and Higher Education, Poland; Istituto Nazionale di Astrofisica (INAF), Italy. This research made use of the Dutch national e-infrastructure with support of the SURF Cooperative (e-infra 180169) and the LOFAR e-infra group. The Jülich LOFAR Long Term Archive and the German LOFAR network are both coordinated and operated by the Jülich Supercomputing Centre (JSC), and computing resources on the supercomputer JUWELS at JSC were provided by the Gauss Centre for Supercomputing e.V. (grant CHTB00) through the John von Neumann Institute for Computing (NIC). This research made use of the University of Hertfordshire high performance computing facility and the LOFAR-UK computing facility located at the University of Hertfordshire and supported by STFC [ST/P000096/1] and Italian LOFAR-IT computing infrastructure supported and operated by INAF, including the resources within the PLEIADI special "LOFAR" project by USC-C of INAF, and by the Physics Department of Turin University (under the agreement with Consorzio Interuniversitario per la Fisica Spaziale) at the C3S Supercomputing Centre, Italy. The PanSTARRS1 Surveys (PS1) and the PS1 public science archive have been made possible through contributions by the Institute for Astronomy, the University of Hawaii, the Pan-STARRS Project Office, the Max-Planck Society and its participating institutes, the Max Planck Institute for Astronomy, Heidelberg and the Max Planck Institute for Extraterrestrial Physics, Garching, The Johns Hopkins University, Durham University, the University of Edinburgh, the Queen's University Belfast, the Harvard-Smithsonian Center for Astrophysics, the Las Cumbres Observatory Global Telescope Network Incorporated, the National Central University of Taiwan, the Space Telescope Science Institute, the National Aeronautics and Space Administration under Grant No. NNX08AR22G issued through the Planetary Science Division of the NASA Science Mission Directorate, the National Science Foundation Grant No. AST-1238877, the University of Maryland, Eotvos Lorand University (ELTE), the Los Alamos National Laboratory, and the Gordon and Betty Moore Foundation. This work is based on observations obtained with XMM-Newton, an ESA science mission with instruments and contributions directly funded by ESA Member States and NASA. This research has made use of SAOImageDS9, developed by Smithsonian Astrophysical Observatory (Joye & Mandel 2003). This research made use of APLpy, an open-source plotting package for Python (Robitaille & Bressert 2012), Astropy, a community-developed core Python package for Astronomy (Astropy Collaboration et al. 2013; Price-Whelan et al. 2018), Matplotlib (Hunter 2007) and Numpy (Harris et al. 2020).

Briggs, D. S. 1995, in American Astronomical Society Meeting Abstracts, Vol. 187, American Astronomical Society Meeting Abstracts, **112**, 02

Brunetti, G., Giacintucci, S., Cassano, R., et al. 2008, *Nature*, **455**, 944

Brunetti, G., Jones, T. W. 2014, *IJMPD*, **23**, 30007

Brunetti, G., Venturi, T., Dallacasa, D., et al. 2007, *ApJ*, **670**, L5

Brunetti, G., Zimmer, S., Zandanel, F. 2017, *MNRAS*, **472**, 1506

Bruno, L., Brunetti, G., Botteon, A., et al. 2023, *A&A*, **672**, A41

Bruno, L., Rajpurohit, K., Brunetti, G., et al. 2021, *A&A*, **650**, A44

Cassano, R. 2010, *A&A*, **517**, A10

Cassano, R. & Brunetti, G. 2005, *MNRAS*, **357**, 1313

Cassano, R., Brunetti, G., & Setti, G. 2006, *MNRAS*, **369**, 1577

Cassano, R., Cuciti, V., Brunetti, G., et al. 2023, *A&A*, **672**, A43

Cassano, R., Ettori, S., Brunetti, G., et al. 2013, *ApJ*, **777**, 141

Cassano, R., Ettori, S., Giacintucci, S., et al. 2010, *ApJ*, **721**, L82

Chambers, K., Magnier, E., Metcalfe, N., et al. 2016, arXiv e-prints, arXiv:1612.05560

Chandra, P., Ray, A., & Bhatnagar, S. 2004, *ApJ*, **612**, 974

Chatterjee, S., Rahaman, M., Datta, A., & Raja, R. 2022, *ApJ*, **164**, 83

Cova, F., Gastaldello, F., Wik, D. R., et al. 2019, *A&A*, **628**, A83

Dahle, H., Kaiser, N., Irgens, R., Lilje, P., & Maddox, S. 2002, *ApJS*, **139**, 313

de Gasperin, F., Dijkema, T. J., Drabent, A., et al. 2019, *A&A*, **622**, A5

Dennison, B. 1980, *ApJ*, **239**, L93

Di Gennaro, G., van Weeren, R. J., Cassano, R., et al. 2021, *A&A*, **654**, A166

Dolag, K. & Enßlin, T. A. 2000, *A&A*, **362**, 151

Ebeling, H., Voges, W., Böhringer, H., et al. 1996, *MNRAS*, **281**, 799

Giacintucci, S., Markevitch, M., Brunetti, G., et al. 2014, *ApJ*, **795**, 73

Giacintucci, S., Markevitch, M., Cassano, R., et al. 2017, *ApJ*, **841**, 71

Giacintucci, S., Venturi, T., Brunetti, G., et al. 2005, *A&A*, **440**, 867

Giacintucci, S., Venturi, T., Cassano, R., Dallacasa, D., & Brunetti, G. 2009, *ApJ*, **704**, L54

Giovannini, G., Bonafede, A., Feretti, L., et al. 2009, *A&A*, **507**, 1257

Govoni, F., Enßlin, T. A., Feretti, L., & Giovannini, G. 2001a, *A&A*, **369**, 441

Govoni, F., Feretti, L., Giovannini, G., et al. 2001b, *A&A*, **376**, 803

Govoni, F., Markevitch, M., Vikhlinin, A., et al. 2004, *ApJ*, **605**, 695

Harris, C. R., Millman, K. J., Van Der Walt, S. J., et al. 2020, *Nature*, **585**, 357

Harwood, J. J., Vernstrom, T., & Stroe, A. 2020, *MNRAS*, **491**, 803

Hoang, D. N., Shimwell, T. W., Osinga, E., et al. 2021, *MNRAS*, **501**, 576

Holjhjem, K., Schirmer, M., & Dahle, H. 2009, *A&A*, **504**, 1

Hunter, J. D. 2007, *Comput. Sci. Eng.*, **9**, 90

Intema, H. T., van der Tol, S., Cotton, W., et al. 2009, SPAM: Source Peeling and Atmospheric Modeling

Joye, W. A. & Mandel, E. 2003, in Astronomical Society of the Pacific Conference Series, Vol. 295, Astronomical Data Analysis Software and Systems XII, ed. Payne, H. E., Jedrzejewski, R. I., & Hook, R. N., **489**

Kale, R., Venturi, T., Giacintucci, S., et al. 2015, *A&A*, **579**, A92

Kale, R., Venturi, T., Giacintucci, S., et al. 2013, *A&A*, **557**, A99

Markevitch, M. & Vikhlinin, A. 2007, *Phys. Rep.*, **443**, 1

Mohan, N. & Rafferty, D. 2015, PyBDSF: Python Blob Detection and Source Finder, Astrophysics Source Code Library

Offringa, A. R., McKinley, B., Hurley-Walker, N., et al. 2014, *MNRAS*, **444**, 606

Offringa, A. R. & Smirnov, O. M. 2017, *MNRAS*, **471**, 301

Osinga, E., van Weeren, R., Brunetti, G., et al. 2024, *Astronomy & Astrophysics*, **688**, A175

Ota, N. & Mitsuda, K. 2004, *A&A*, **428**, 757

Owen, F., Morrison, G., & Voges, W. 1999, in Diffuse Thermal and Relativistic Plasma in Galaxy Clusters, ed. Boehringer, H., Feretti, L., & Schuecker, P., **9**

Pasini, T., De Gasperin, F., Brüggen, M., et al. 2024, *A&A*, **689**, A218

Planck Collaboration XXVII. 2016, *A&A*, **594**, A27

Press, W. & Schechter, P. 1974, *ApJ*, **187**, 425

Price-Welan, A. M., Sipőcz, B., Günther, H., et al. 2018, *ApJ*, **156**, 123

Rizza, E., Burns, J. O., Ledlow, M. J., et al. 1998, *MNRAS*, **301**, 328

Robitaille, T. P. & Bressert, E. 2012, APLpy: Astronomical Plotting Library in Python, Astrophysics Source Code Library

Santra, R., Kale, R., Giacintucci, S., et al. 2024, *The Astrophysical Journal*, **962**, 40

Savini, F., Bonafede, A., Brüggen, M., et al. 2018, *MNRAS*, **478**, 2234

Shimwell, T. W., Hardcastle, M. J., Tasse, C., et al. 2022, *A&A*, **659**, A1

Shimwell, T. W., Tasse, C., Hardcastle, M. J., et al. 2019, *A&A*, **622**, A1

Smirnov, O. M. & Tasse, C. 2015, *MNRAS*, **449**, 2668

Springel, V., Frenk, C. S., & White, S. D. 2006, *Nature*, **440**, 1137

Starck, J.-L. & Pierre, M. 1998, *Astronomy and Astrophysics Supplement Series*, **128**, 397

Tasse, C. 2014a, arXiv e-prints [arXiv:1410.8706]

Tasse, C. 2014b, *A&A*, **566**, A127

Tasse, C., Hugo, B., Mirmont, M., et al. 2018, *A&A*, **611**, A87

Tasse, C., Shimwell, T. W., Hardcastle, M. J., et al. 2021, *A&A*, **648**, A1

van Haarlem, M., Wise, M. W., Gunst, A., et al. 2013, *A&A*, **556**, A2

van Weeren, R., Timmerman, R., Vaider, V., et al. 2024, *A&A*, **692**, A12

van Weeren, R. J., de Gasperin, F., Akamatsu, H., et al. 2019, *Space Sci. Rev.*, **215**, 16

van Weeren, R. J., Shimwell, T. W., Botteon, A., et al. 2021, *A&A*, **651**, A115

van Weeren, R. J., Williams, W. L., Hardcastle, M. J., et al. 2016, *ApJS*, **223**, 2

Vazza, F. & Botteon, A. 2024, *Galaxies*, **12**, 19

Venturi, T., Giacintucci, S., Brunetti, G., et al. 2007, *A&A*, **463**, 937

Venturi, T., Giacintucci, S., Dallacasa, D., et al. 2008, *A&A*, **484**, 327

Wen, Z. & Han, J. 2013, *MNRAS*, **436**, 275

Wilber, A. G., Brüggen, M., Bonafede, A., et al. 2018, *MNRAS*, **473**, 3536

Williams, W. L., van Weeren, R. J., Röttgering, H. J., et al. 2016, *MNRAS*, **460**, 2385

Xie, C., van Weeren, R. J., Lovisari, L., et al. 2020, *A&A*, **636**, A3

Zhang, X., Simionescu, A., Gastaldello, F., et al. 2023, *A&A*, **672**, A42

References

Abell, G., Corwin Jr., H., & Olowin, R. 1989, *ApJS*, **70**, 1

Adam, R., Goksu, H., Brown, S., Rudnick, L., & Ferrari, C. 2021, *A&A*, **648**, A60

Allen, S., Schmidt, R., Fabian, A., & Ebeling, H. 2003, *MNRAS*, **342**, 287

Astropy Collaboration, Robitaille, T. P., Tollerud, E. J., et al. 2013, *A&A*, **558**, A33

Balboni, M., Gastaldello, F., Bonafede, A., et al. 2024, *A&A*, **686**, A5

Barrena, R., Boschin, W., Girardi, M., & Spolaor, M. 2007, *A&A*, **467**, 37

Barrena, R., Girardi, M., Boschin, W., De Grandi, S., & Rossetti, M. 2014, *MNRAS*, **442**, 2216

Biava, N., Bonafede, A., Gastaldello, F., et al. 2024, *A&A*, **686**, A82

Blasi, P. & Colafrancesco, S. 1999, *Astropart. Phys.*, **12**, 169

Böhringer, H., Voges, W., Huchra, J. P., et al. 2000, *ApJS*, **129**, 435

Bonafede, A., Intema, H. T., Brüggen, M., et al. 2014, *MNRAS*, **444**, L44

Botteon, A., Shimwell, T. W., Cassano, R., et al. 2022, *A&A*, **660**, A78

Appendix A: LOFAR model injection of radio halos

Injection of the real LOFAR model of A773 RH into the uGMRT image at a position offset from the center without any artifacts.

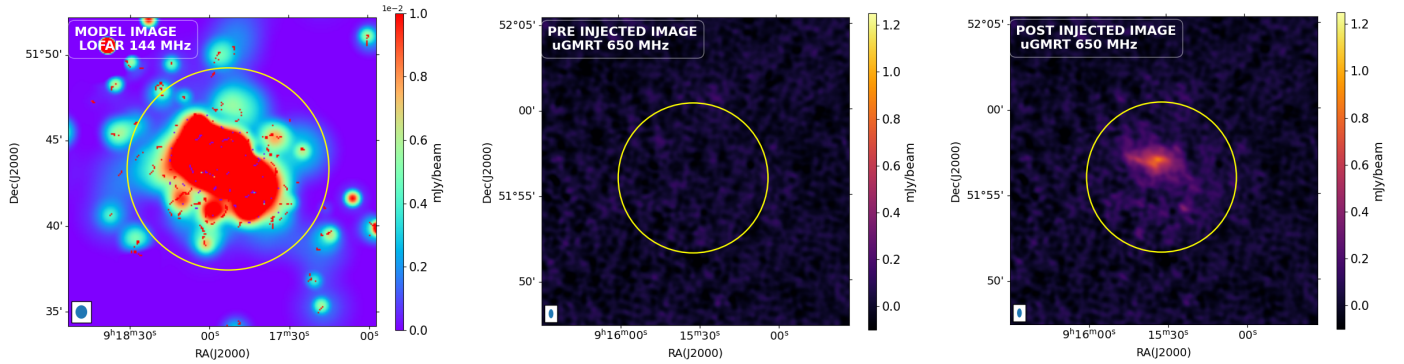


Fig. A.1: Real LOFAR model injection into a uGMRT image. *From left to right:* LOFAR source-subtracted model image tapered at 100 kpc (144 MHz), with the yellow region indicating the area chosen for injection; uGMRT source-subtracted image (650 MHz) before injection at the designated RA and DEC; uGMRT source-subtracted image after injection of the LOFAR model rescaled at 650 MHz with $\alpha = -1$, with the yellow region representing the size of the halo recovered after the injection.

Appendix B: Distribution of α in the SI map

Histogram showing the distribution of spectral index (α) values from the SI map in Fig. 5. The α values were averaged within radio beam sized boxes across the map and plotted for regions above the 3σ and 5σ contours.

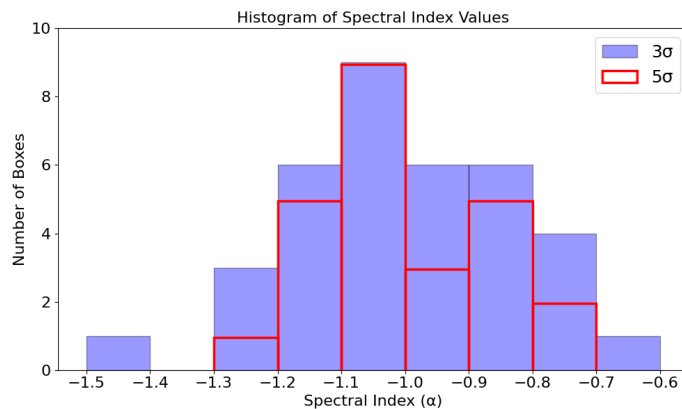


Fig. B.1: Distribution of spectral index (α) values in A773, measured within radio beam sized boxes ($50'' \times 50''$). Blue and red bins represent regions with flux densities above $3\sigma_{rms}$ and $5\sigma_{rms}$, respectively.

Appendix C: Point to point analysis

The region of interest for the point-to-point analysis was divided into boxes with areas equivalent to the beam size, ensuring that the measurements are independent. The radio (I_{radio}) and X-ray surface brightness (I_X) were extracted for these grid cells and subsequently used for the point-to-point correlation analysis (see Fig 8). Shown here are the sampling grids used for A773 and A1351, overlaid on both the LOFAR and uGMRT images.

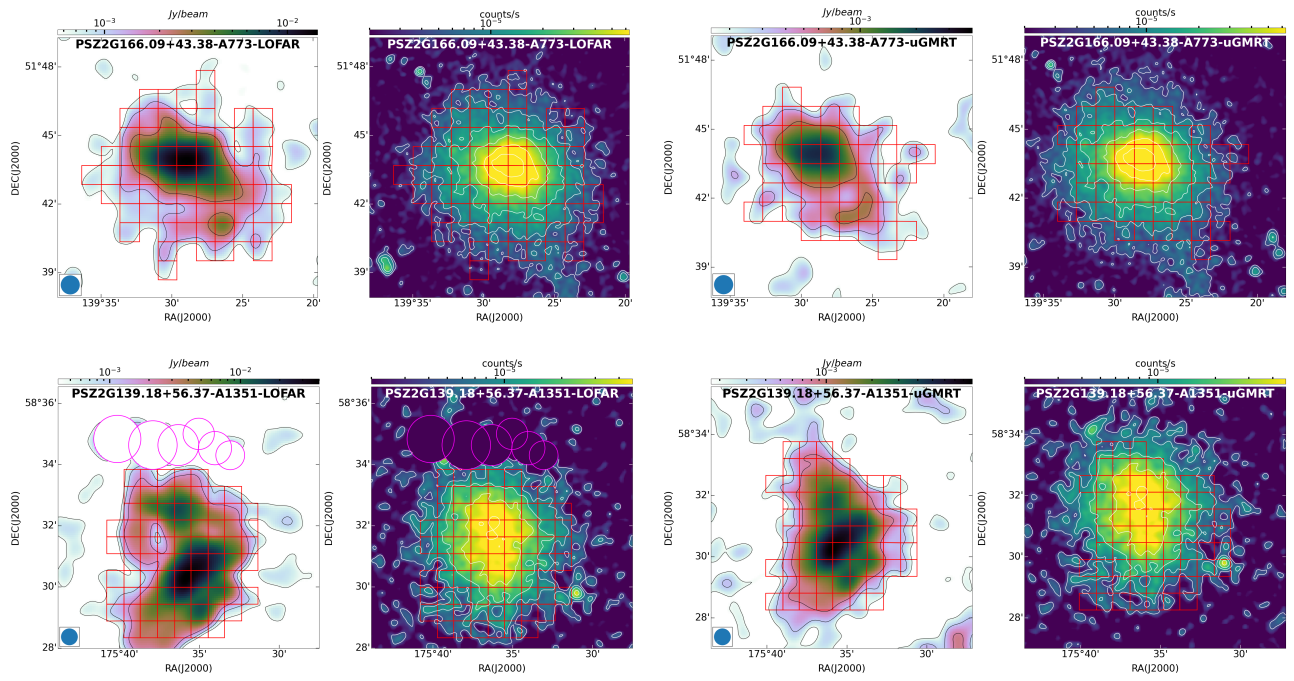


Fig. C.1: *Left to right:* LOFAR source subtracted image of A773 at a resolution of $50'' \times 50''$ compared with X-ray XMM image, uGMRT source subtracted image of A773 at a resolution of $50'' \times 50''$ compared with X-ray XMM image, LOFAR source subtracted image of A1351 at a resolution of $33'' \times 33''$ compared with X-ray XMM image, uGMRT source subtracted image of A1351 at a resolution of $33'' \times 33''$ compared with X-ray XMM image. The boxes indicate the corresponding regions where radio and X-ray brightness were compared, and the circles indicate the masked regions in radio and X-ray images.